Available online at www.sciencedirect.com
ScienceDirect
Trans. Nonferrous Met. Soc. China 32(2022) 3985−3997
Transactions of Nonferrous Metals Society of China
www.tnmsc.cn

Plasma electrolytic oxidation behavior and corrosion resistance of brass in aluminate electrolyte containing NaH_2PO_4 or Na_2SiO_3

Yu-lin CHENG, Tian FENG, Jia-hui LÜ, Pan-feng HU, Ying-liang CHENG

College of Materials Science and Engineering, Hunan University, Changsha 410082, China

Received 30 September 2021; accepted 3 January 2022

Abstract: Plasma electrolytic oxidation (PEO) of brass was carried out in aluminate electrolytes with the addition of NaH_2PO_4 (S1) and Na_2SiO_3 (S2), respectively, with the aim to investigate the effect of additives on the coating formation and corrosion resistance. For the PEO in S1 electrolyte, a mixed layer of $AlPO_4$ and Al_2O_3 is formed at the initial stage, which leads to fast plasma discharges and formation of black coatings with the compositions of Al_2O_3, CuO, Cu_2O and ZnO. However, in S2 electrolyte, plasma discharges are delayed and the coatings show a reddish color due to more Cu_2O. Mott−Schottky tests show that the S1 coatings are p-type semiconductors; while the S2 coatings can be adjusted between n-type and p-type. Potentiodynamic polarization and electrochemical impedance spectroscopy (EIS) tests show that the PEO treatment can significantly improve the corrosion resistance of brass, with protection efficiency up to 91.50% and the largest charge transfer resistance of 59.95 kΩ·cm^2 for the S1 coating.
Key words: plasma electrolytic oxidation; brass; corrosion resistance; aluminate; sodium dihydrogen phosphate; sodium silicate

1 Introduction

Owing to good mechanical and electrical properties of copper and its alloys, they can be applied to many sectors of human life, such as power generation, electrical industries and military uses [1−3]. However, poor strength, hardness, tribological and corrosion properties of copper and its alloys restrict their practical applications [1,4]. Therefore, it is necessary to overcome these disadvantages through surface engineering or other methods.

Plasma electrolytic oxidation (PEO), also called micro-arc oxidation (MAO), is an advanced surface modification technique which can be employed to treat valve metals and its alloys (Al, Mg, Ti, Zr and Ta, etc.) to improve their biocompatibility, decorative function, wear and corrosion resistances [5−10]. However, recently, there have also been a few reports about the PEO of non-valve metals such as carbon steel, brass and copper [11−14]. In the PEO treatment, oxides are generated on the metal surface by oxidation of the substrate and the decomposition of the electrolyte species due to the high temperature plasma discharges. Oxides of CuO, Cu_2O and ZnO can be formed during the PEO of brass, which enhance the wear performance of the alloy [13]. Besides, these oxides are advanced materials with multi-functional applications [15−17]. For example, CuO and Cu_2O are typical p-type semiconductors with a narrow band gap of 1.2−1.8 and 1.9−2.2 eV, respectively. Due to the non-toxicity, good stability and electrochemical activity, CuO has great application prospects in catalytic, conduction, gas sensing and electrode materials [18−20]. Cu_2O could also be used in solar cell, antibacterial properties and wastewater treatment [21−23]. ZnO is an n-type semiconductor material with a band gap

Corresponding author: Ying-liang CHENG, Tel: +86-731-88821727, Fax: +86-731-88823554, E-mail: chengyingliang@hnu.edu.cn
DOI: 10.1016/S1003-6326(22)66072-2

of ~3.4 eV, which can be used as a gas sensing for the eco-friendliness and good stability [24−26].

In our previous work [13], we demonstrated that brass can be PEO-treated in silicate electrolyte to form wear-resistant coatings, but corrosion resistance of the coatings fabricated in that electrolyte has not been reported yet. Besides, the formation mechanism of PEO coatings on copper has been investigated in aluminate-based electrolytes with respective additives of Na_3PO_4, NaH_2PO_4 and NaH_2PO_2, showing that the additives significantly modified the coating formation mechanism [14]. As we all know, aqueous-based alkaline electrolytes, such as aluminate [10,27,28], phosphate [29−32], silicate [5,7] or their mixed electrolytes [33,34] are widely used in PEO study. The coating formation mechanism may be also modified with the application of different electrolytes. Hence, it is meaningful to carry out PEO of brass in a variety of electrolytes, with the aim to explore the coating formation mechanism and properties of the formed coatings.

In this work, PEO of brass was carried out in aluminate electrolytes with the addition of sodium dihydrogen phosphate (NaH_2PO_4) or sodium silicate (Na_2SiO_3). The coating formation processes were investigated by monitoring the cell potential− time curves. Characterization methods of SEM, XRD, and XPS were adopted to analyze the surface of the PEO coatings. Mott−Schottky test was used to investigate the semiconductor type of coatings formed in different electrolytes. The corrosion resistance of coatings was evaluated by electrochemical methods.

2 Experimental

2.1 Sample preparation

A ~2 mm thick plate of brass with a nominal composition (mass fraction) of 56% Cu and 44% Zn was cut and mounted in epoxy resin to expose an area of 10 mm × 10 mm. The specimens were polished from 600# to 2000# grit SiC paper, and the experimental setup for PEO was the same as that depicted in Ref. [5]. Two kinds of electrolytes with the compositions of 8 g/L $NaAlO_2$ + 2 g/L $NaH_2PO_4{\cdot}2H_2O$ (named as "S1") and 8 g/L $NaAlO_2$ + 5 g/L $Na_2SiO_3{\cdot}9H_2O$ (named as "S2") were used in this study. The electrolytes were prepared using distilled water and analytical grade reagents (Sinopharm Co., Ltd.). A 5 kW power source (Pulsetech Electrical Co., Ltd., Chengdu, China) was used for the PEO treatment. An oscilloscope (Tektronix TDS 1002CSC) was used to monitor the waveforms during the PEO processing. During the PEO processing, pulsed unipolar regime with a frequency of 2000 Hz and a duty cycle of 5% was employed. Average current densities of ~0.21 and ~0.32 A/cm^2 were used in the electrolytes of S1 and S2, respectively (higher current density is beneficial to the occurrence of plasma discharges in S2).

2.2 Characterization

The surface and cross-sectional morphologies of the coatings were examined by scanning electron microscopy (SEM, Nova Nano 230, FEI) equipped with energy-dispersive spectrometer (EDS). The phase composition of the PEO coatings was tested by X-ray diffraction (XRD, Rigaku D/MAX 2500 diffractometer, Cu K_α radiation, scan range from 20° to 100° in 2θ and a step of 8 (°)/min). The chemical states of the surface of coatings were examined by X-ray photoelectron spectroscopy (XPS, ThermoFisher-VG Scientific, USA), with Al K_α radiation as the excitation source. All XPS data were corrected to a polluted C 1s peak at binding energy of 285.0 eV.

An electrochemical workstation (CHI 660B) equipped with a three-electrode set-up was adopted to conduct Mott−Schottky (M−S) and corrosion tests of samples. A piece of platinum and a saturated calomel electrode (SCE) were used as the auxiliary and reference electrodes, respectively, and the specimens (substrate and coatings) were used as the working electrode. Prior to electrochemical tests, the open circuit potential (OCP) was recorded for 3600 s to obtain a steady-state. The M−S test was registered in 3.5 wt.% NaCl solution at a frequency of 1 kHz and a sweep rate of 20 mV/s, and a sweeping potential range from 0 to −0.7 V. The electrochemical impedance spectroscopy (EIS) measurement was carried out at the OCP over a frequency range from 100 kHz to 0.005 Hz at a sinusoidal amplitude potential perturbation of 10 mV. And then the potentiodynamic polarization tests were conducted in 3.5 wt.% NaCl solution in the potential range from −0.5 to +1 V with respect to the OCP, at a scan rate of 1 mV/s. Each electrochemical experiment was repeated more than three times to ensure reproducibility.

3 Results

3.1 PEO behavior of brass in S1 and S2

3.1.1 Cell potential−time curves and optical pictures

Figures 1(a) and (b) show the cell potential−time curves as function of time and corresponding optical appearances of brass samples formed at different potentials in S1 and S2 electrolytes, respectively. In S1 electrolyte (Fig. 1(a)), the curve can be divided into two parts: (i) rapid rise part (0−30 s); (ii) slow near linear growth part (30−600 s), which is similar to that of the potential behavior in valve metals [5]. Only the edge of the sample is covered by black coating material at 600 V and 20 s; however, uniform coating is eventually formed on the whole sample surface in part (ii) as the cell potential goes up. The cell potential curve behaves differently in S2. There are three parts in the curve in Fig. 1(b), among which an intermediate transition part of ~350 s is evident.

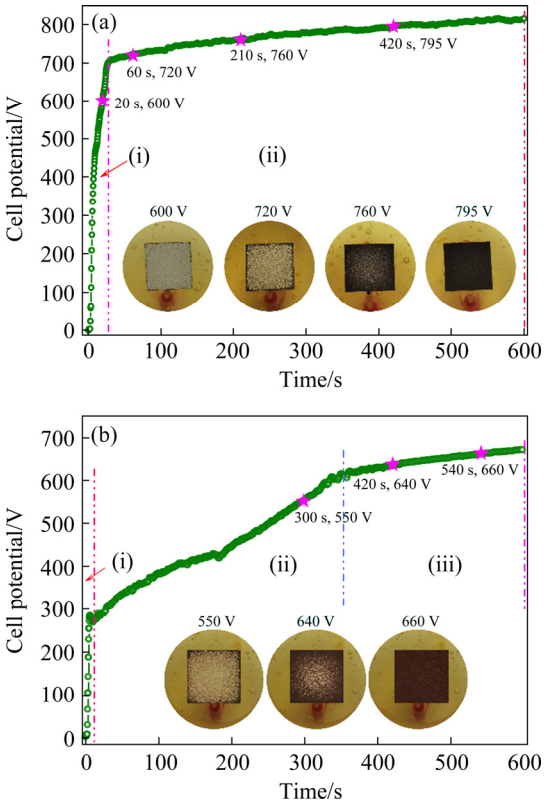

Fig. 1 Cell potential−time responses during PEO of brass for 600 s and appearances of samples formed at different stages: (a) In S1 electrolyte at current density of 0.21 A/cm^2; (b) In S2 electrolyte at current density of 0.32 A/cm^2

The trend of this curve is similar to that of PEO of brass in pure silicate electrolyte [13], which shows the slow rise of cell potential and delayed occurrence of plasma spark discharge. In Fig. 1(b), it has taken a long time (~300 s) to produce the spark discharges at the edge of the sample under a potential of ~550 V. In part (iii), discharges and coatings gradually covered the whole surface of the sample. There is a common phenomenon in Fig. 1 that the coatings is formed preferentially at the corners of the samples, and then gradually covers the centre. The difference is that a black coating is finally generated in S1 electrolyte, nevertheless, a reddish brown coating is formed in S2 electrolyte which is similar to the coating formed in pure silicate [13].

3.1.2 Morphologies of surface and cross-sections of coatings in S1

Figures 2(a−d) display the SEM images for the surface of the representative samples selected from Fig. 1(a). The EDS analysis data of Areas 1 to 5 in Fig. 2 are listed in Table 1. Figure 2(a) shows the centre area of the sample formed at 600 V; at this stage, an irregularly thin film has covered on the surface. According to the EDS analyses, it is found that no P was detected in Area 1, but a large amount of Cu and Zn and a certain amount of O were detected (Table 1), which indicates that the oxide film has not yet been formed in Area 1. However, a small amount of P was detected in Area 2. This also proves that the formation of $AlPO_4$ is a prerequisite for spark discharges [14]. Compared with Area 1, the contents of Cu and Zn were decreased, and the contents of O and Al in Area 2 were increased. The inset image in Fig. 2(a) is the edge morphology of the sample, which shows the coexistence morphologies of “dried-up river bed” and discharge channels. At 720 V, due to the same surface morphologies of the centre and edge of the coating, only the central image displays in Fig. 2(b). A “dried-up river bed” morphology featured by numerous “footprints” of discharges and cracks also presents on the brass surface, which is the same as that of PEO of carbon steel and copper [11,14]. When the cell potential rises to 760 V, the surface morphology of the edge presents a typical PEO feature with discharge channels (image not shown), while some “dried-up river bed” morphologies still exist in the centre region (Fig. 2(c)). As the cell potential rises to 795 V, the surface of the sample

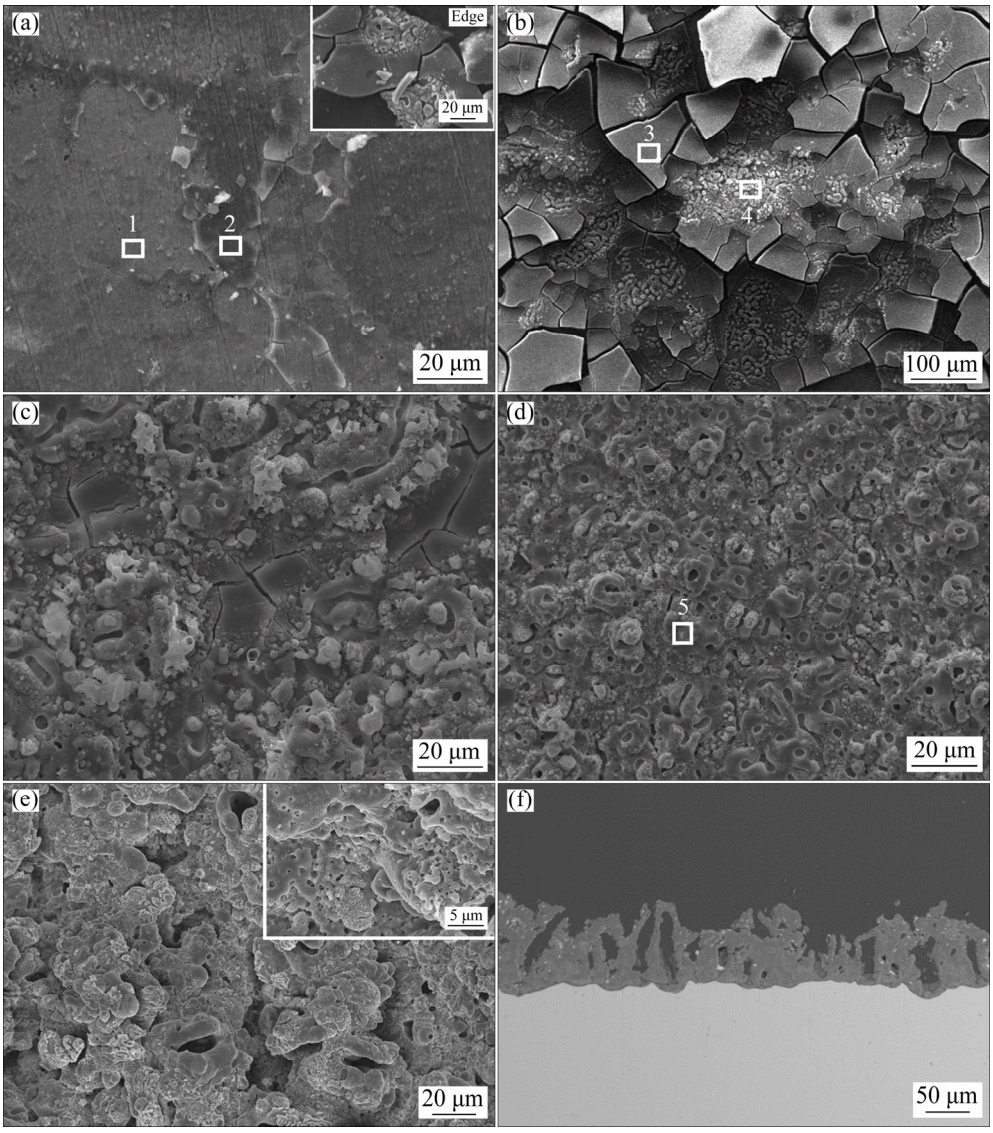

Fig. 2 SEM images of PEO-treated samples formed in S1 electrolyte at different time: (a) 20 s, 600 V, centre; (b) 60 s, 720 V, centre; (c) 210 s, 760 V, centre; (d) 420 s, 795 V; (e, f) 1800 s, 876 V

Table 1 EDS analysis data of different areas in Fig. 2 (at.%)

Area No.	Cu	Zn	O	Al	P
1	44.92	25.19	24.93	4.96	–
2	14.93	8.30	55.21	19.64	1.92
3	0.70	0.44	58.83	31.94	8.09
4	4.87	2.10	52.11	34.38	6.54
5	5.22	3.01	55.50	29.27	7.00

has been completely covered by the coating (Fig. 1(a)), showing a PEO appearance caused by spark discharges (Fig. 2(d)), with the morphology similar to the coating formed at 760 V. When the cell potential increases from 720 to 795 V, the contents of Cu, Zn, O and P in the discharge channels (Areas 4 and 5) have increased (Table 1). It can be observed that a lots of small discharge holes are attached around the large holes in the inset image of Fig. 2(e), which has confirmed the A-type or C-type discharges [35]. An ~80 μm thick coating with large discharge channels is formed after 1800 s PEO processing (Fig. 2(f)).

3.1.3 Morphologies of surface and cross-sections of coatings in S2

The SEM images for the surface of the representative samples selected from Fig. 1(b) are shown in Figs. 3(a–c). The EDS analysis data from Areas *A* to *D* in Fig. 3 are listed in Table 2. At 550 V, there are a few “dried-up river bed” morphologies and large patches of coating with numerous small pores of spark discharge channels in the centre

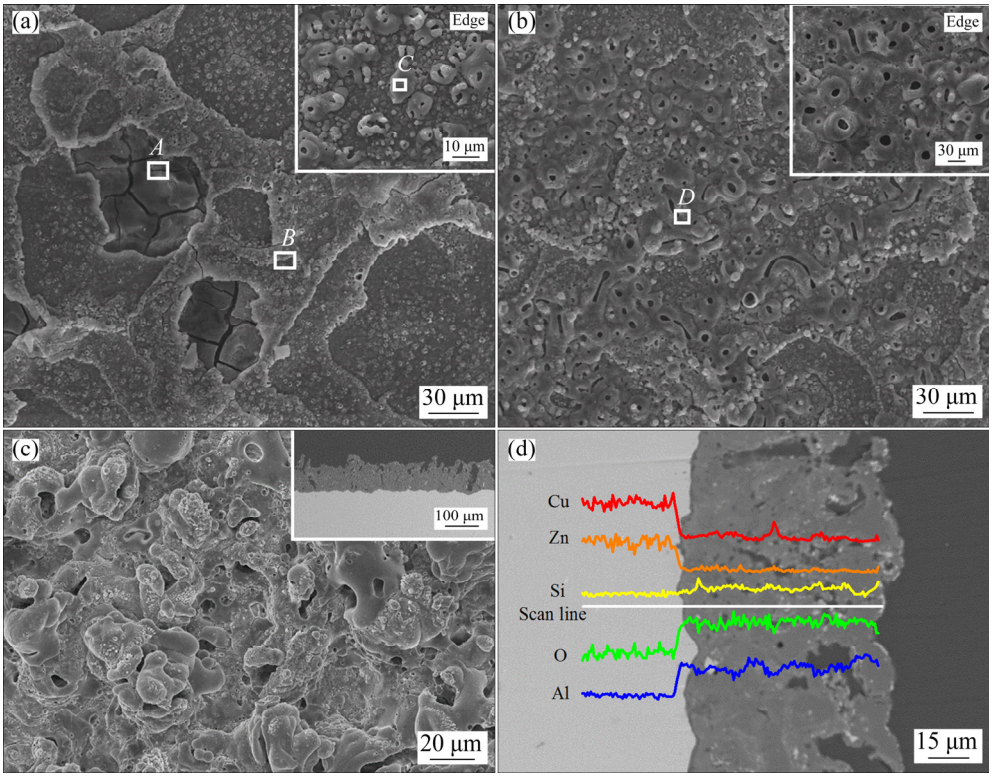

Fig. 3 SEM images (a−c) and elemental scanning mapping (d) of PEO-treated samples formed in S2 electrolyte at different time: (a) 300 s, 550 V, centre; (b) 420 s, 640 V, centre; (c, d) 1800 s, 870 V

Table 2 EDS analysis data of different areas in Fig. 3 (at.%)

Area No.	Cu	Zn	O	Al	Si	Na
A	1.42	0.81	64.03	28.78	4.96	−
B	2.60	1.47	51.67	33.42	10.77	0.07
C	10.31	6.23	43.78	32.41	7.27	−
D	2.40	0.84	49.45	38.04	7.88	1.39

region of the sample surface (Fig. 3(a)), while the "dried-up river bed" morphology disappears and the size of the discharge channels become larger at the edge of coatings (the inset image in Fig. 3(a)). As shown in Table 2, it can be found that the contents of Cu, Zn, Al and Si in the "dried-up river bed" morphology are less than those of the morphology with fine discharges, which illustrates that the "dried-up river bed" morphology is mainly due to the material deposition. In Fig. 3(b), the central region of the coating formed at 640 V has a similar morphology to the edge area at 550 V (the inset image in Fig. 3(a)), showing the coexistence of small and large discharge channels. The EDS analysis data in Table 2 show that the element contents of the small discharge channels (Area *B*) are similar to those of large discharge channels (Area *D*). When the cell potential increases to 660 V, the coating covers the entire brass surface (Fig. 1(b)), and the morphology has no obvious difference from the edge region of 640 V. Further, with the PEO time increasing, the surface morphology of the coating formed at 1800 s in S2 (Fig. 3(c)) basically presents the same as the coatings formed in S1 (Fig. 2(e)). While as shown in the inset picture of Fig. 3(c), the thickness of the coating is ~65 μm after 1800 s PEO treatment, which indicates that the coating growth rate in S2 is slower than that in S1 (~80 μm). The result of EDS line scan across the coating shows that the Cu, Zn, Al, Si, O and P elements are distributed uniformly in the cross-section (Fig. 3(d)).

3.2 XRD patterns

In Fig. 4, the phase compositions of the coatings formed at 1200 s in S1 and S2 have been investigated by XRD. The peaks of Cu and $(Cu_{13}Zn_{17})_{0.2}$ are detected in both curves, which come from the substrate. The CuO, Cu_2O and ZnO phases are also detected in Fig. 4, which is consistent with the EDS results. Further, the

coatings contain γ-Al_2O_3 and a little α-Al_2O_3, which origin from the electrolyte. Judging from the number and relative intensity of corresponding peaks in the XRD spectra, the contents of CuO, α-Al_2O_3 and γ-Al_2O_3 in coatings formed in S1 may be higher than those of coatings formed in S2. It is worth noting that a broad peak between 20° and 40° is observed in the S2 curve, which may be attributed to the amorphous material of SiO_2, since a great content of Si is detected by EDS (Table 2) and also some studies have reported the presence of amorphous SiO_2 [13,36,37].

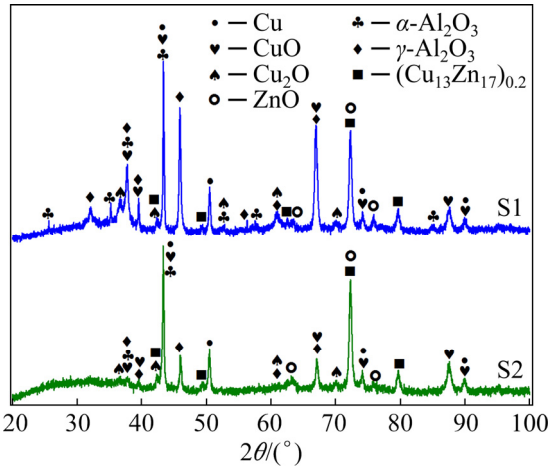

Fig. 4 XRD patterns of oxide coatings formed at 1200 s for PEO in S1 and S2

3.3 XPS spectra

As shown in Fig. 5, X-ray photoelectron spectroscopy (XPS) was applied to characterizing the valence states of Cu, Zn, Al, O and Si for the coatings formed in the S1 and S2 electrolytes after 1200 s PEO processing, respectively. In Fig. 5(a), the Cu 2p spectrum of the sample formed in S1 can be attributed to Cu_2O and CuO. A doublet separation of CuO peaks located at 934.48 and 954.58 eV, and another doublet separation of Cu_2O peaks located at 932.55 and 952.49 eV can be found for the Cu 2p scan in S1 [13,14]. The satellite peaks of Cu^{2+} [14] are also be found in the spectrum of S1. In the spectrum of the coating formed in S2 electrolyte, the CuO peaks and its satellite peaks are not observed, only showing the peaks from Cu_2O. The result shows that content of CuO must be very low on the surface of S2 coating, although it was detected in the XRD pattern (Fig. 4). This is also consistent with reddish color of the coating, since Cu_2O is a material with bright red color. In Fig. 5(b), the high resolution Zn 2p spectrum shows a doublet separation of ZnO peaks at 1021.74 and 1044.84 eV, which can be assigned to Zn $2p_{1/2}$ and Zn $2p_{3/2}$ [13], respectively. The gap of binding energy between the two peaks is 23.10 eV. As shown in Fig. 5(c), the Al 2p spectra in S1 can be deconvoluted into three peaks at 74.16, 76.55 and 78.51 eV, respectively. The peaks at 74.16 and 76.55 eV correspond to α-Al_2O_3 (74.16 eV in Ref. [5]) and γ-Al_2O_3 (76.44 eV in Ref. [5]), respectively. The deconvoluted peak at 78.51 eV may correspond to the unknown species with the peak binding energy of 78.97 eV as found in Ref. [38]. Whereas, only the peaks of α-Al_2O_3 and γ-Al_2O_3 are found in the coating formed in S2 electrolyte. Figure 5(d) shows the O 1s spectra of the coatings formed in the two electrolytes. The spectra can be deconvoluted into four peaks at 530.12, 530.85, 531.59 and 532.60 eV in S1, corresponding to CuO (530.20 eV in Ref. [39]), ZnO (530.80 eV in Ref. [40]), Al_2O_3 (531.24 eV in Ref. [38]) and Cu_2O (532.51 eV in Ref. [41]), respectively. However, an additional peak of SiO_2 is matched at 532.89 eV (533.00 eV in Ref. [42]) in S2 electrolyte, which is consistent with the EDS and XRD results. Also, the Si 2p spectrum (Fig. 5(e)) shows the binding energy of 101.86 eV, which is close to 102.08 eV in Ref. [13]. The above results further demonstrate that substrate elements (i.e. Cu and Zn) and also electrolyte species have participated in the coating formation process, resulting in copper/zinc-containing oxide coatings on the surface of brass.

3.4 M−S test results

In general, Mott−Schottky theory (M−S) is a simple method which can obtain a great amount of information about semiconductive materials, such as the type of charge carriers, the value of the flat-band potential (φ_{fb}) and the charge carrier density [43−45]. Electrons as the dominative charge carriers within the space charge region are n-type semiconductors, while holes more than electrons are p-type materials [46]. In M−S plots, the slope is negative for p-type semiconductors and positive for n-type semiconductors [45], and the φ_{fb} value is the intersection of the slope and the ordinate ($C^{-2}=0$, C is the space-charge capacitance) [47].

The M−S plots of coatings formed in S1 and S2 at 1200 s are shown in Fig. 6. In the sweeping potential range from 0 to −0.7 V, the M−S curve of

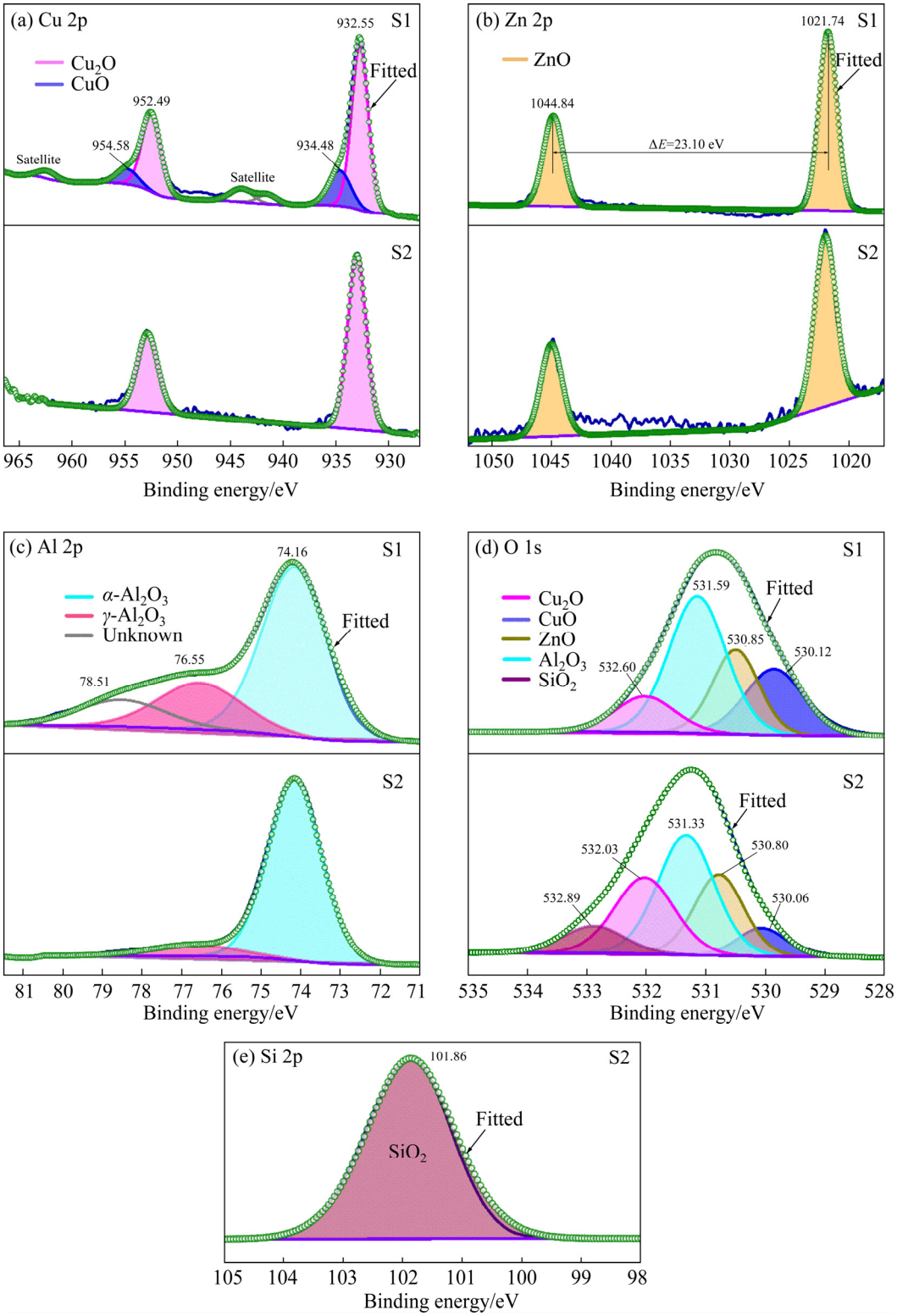

Fig. 5 High-resolution XPS spectra for samples after 1200 s PEO treatment in S1 and S2: (a) Cu 2p; (b) Zn 2p; (c) Al 2p; (d) O 1s; (e) Si 2p

the oxide coating formed in S1 shows p-type characteristics from −0.33 to 0 V (Fig. 6(a)). The p-type behavior may be due to a higher CuO content in the coating. The φ_{fb} value is −0.01 V which is extracted from Fig. 6(a). However, in Fig. 6(b), the M−S plot of the coatings formed in S2 electrolyte shows both n-type (< −0.28 V) and p-type characteristics (> −0.28 V). The φ_{fb} values

are −0.78 and −0.01 V which are derived from the n-type and p-type branches, respectively. The curve in Fig. 6(b) shows the n-type characteristics, which may be caused by the combination of a certain amount of ZnO in the coating and electron enrichment on the coating surface due to the reduction of applied potential [14,48]. When the applied potential is higher than −0.28 V, it seems to show p-type semiconductor behavior probably because the coating contains some p-type oxides, such as CuO and Cu_2O.

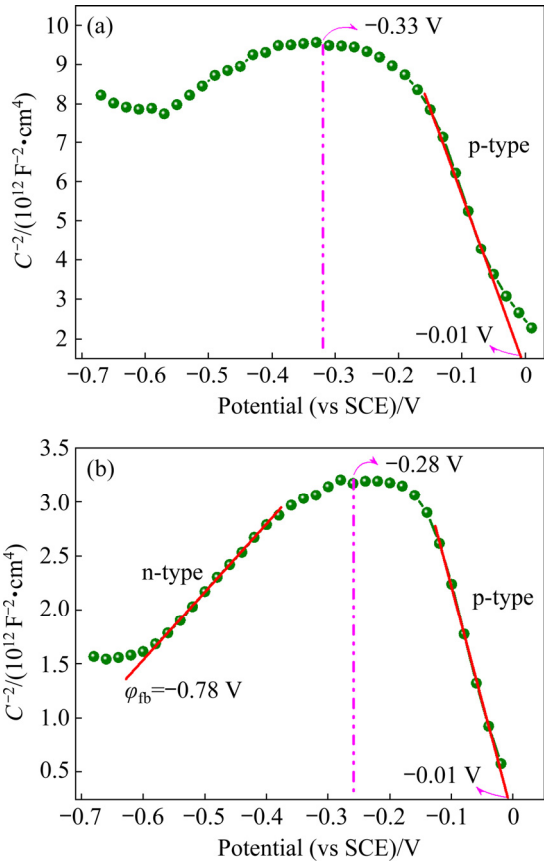

Fig. 6 Mott−Schottky plots of coatings formed at 1200 s in S1 (a) and S2 (b) electrolytes, respectively

3.5 Corrosion resistance

3.5.1 Polarization curve

The polarization curves of brass and the coatings prepared in S1 and S2 electrolytes have been obtained in 3.5% NaCl solution (Fig. 7). The anodic current density of the brass increases sharply at the potential of −0.1 V, which indicates the occurrence of pitting corrosion. However, the pitting corrosion occurs at a higher potential of 0 V for the coating formed in S2 electrolyte, and there is no obvious pitting behavior for the coating formed in coating formed in S1. Furthermore, the anodic polarization curve of S1 displays a region of passivation between 0.1 and 0.35 V. The Tafel extrapolation was employed to obtain the free corrosion current density from the polarization curves [47]. The data are recorded in Table 3. The protection efficiency (η, %) of the oxide coatings on the substrate is further calculated from Eq. (1) [49,50]:

$$\eta=\frac{J_{corr(o)}-J_{corr(i)}}{J_{corr(o)}}\times 100\% \quad (1)$$

where $J_{corr(o)}$ and $J_{corr(i)}$ are the respective corrosion current densities of the uncoated brass and coatings formed in S1 and S2 electrolytes.

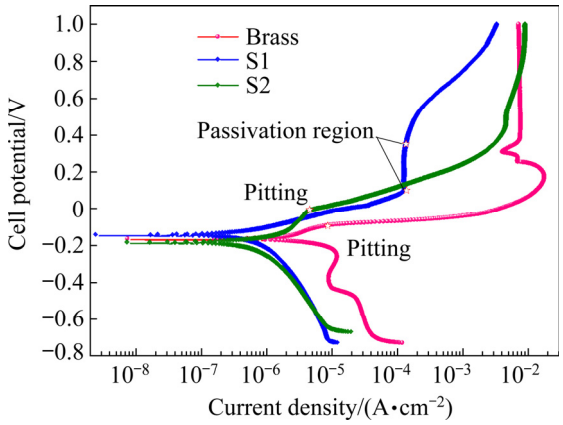

Fig. 7 Potentiodynamic polarization curves in 3.5 wt.% NaCl solution for uncoated brass and coatings obtained by PEO treatment in S1 and S2 for 1200 s, respectively

Table 3 Comparison of corrosion resistance data of potentiodynamic polarization curves of uncoated brass and coatings formed in S1 and S2 electrolytes

Sample	J_{corr}/(A·cm^{-2})	φ_{corr}(vs SCE)/V	η/%
Brass	7.68×10^{-6}	−0.17	−
S1 coating	6.53×10^{-7}	−0.15	91.50
S2 coating	6.97×10^{-7}	−0.19	90.92

According to Table 3, the free corrosion current densities (J_{corr}) and corrosion potentials (φ_{corr}) are respectively 7.68×10^{-6} A/cm^2 and −0.17 V for the uncoated brass, and 6.53×10^{-7} A/cm^2 and −0.15 V for S1 coating, and 6.97×10^{-7} A/cm^2 and −0.19 V for S2 coating. It can be seen that the corrosion current densities of the coatings prepared in S1 and S2 electrolytes are an order of magnitude lower than that of the uncoated brass, and the corrosion protection effect of coatings formed in S1 and S2 electrolytes are 91.50% and

90.92%, respectively. The data indicate that these two coatings can offer good protection to the substrate. However, the corrosion resistance of the S1 coating may be better since the coating does not show pitting corrosion and owns a passive region in the anodic polarization curve.

3.5.2 EIS data

EIS test was also carried out to evaluate the corrosion resistance of samples, with the aim to reveal more details during the corrosion processing [49]. Figure 8 shows the EIS test results of uncoated brass and coatings formed in S1 and S2 electrolytes. It can be seen from the Nyquist plots (Fig. 8(a)) that the capacitive arc diameter of the S1 coating is the largest and that of the substrate is the smallest. A larger diameter of the capacitive arc normally means better corrosion protection performance [2,51]. Therefore, it can be concluded that the coatings prepared in S1 and S2 electrolytes have good protection to the substrate, with S1 coating being the best.

Figures 8(b) and (c) show the Bode modulus and phase angle plots, respectively. In the Bode modulus plots, the modulus value at low frequency can directly represent the corrosion resistance of samples, that is, the larger the modulus, the stronger the corrosion resistance [49]. Although the moduli of the substrate and coating in the low frequency region are of the same order of magnitude (~10^4), the modulus value of the coating generated in S1 electrolyte is the largest, and modulus value of uncoated brass is the lowest, which are consistent with Nyquist plots (Fig. 8(a)). In Fig. 8(c), the plots of phase angle show two humps in the middle-high frequency range and the low frequency range, respectively, which indicates two-time constants in the system. For the brass with PEO coatings, the time constant in the middle-high frequency region represents the relaxation process of the coating, while the time constant in low frequency region is correlated with the charge transfer at interface of the metal and the coating pores which are filled with electrolyte [49,52].

The EIS data were fitted by a two-time constant equivalent circuit in Fig. 8(d) for bare brass and also the coated samples. Although the surface of the brass is not covered with a PEO coating, there is also a very thin oxide film on the

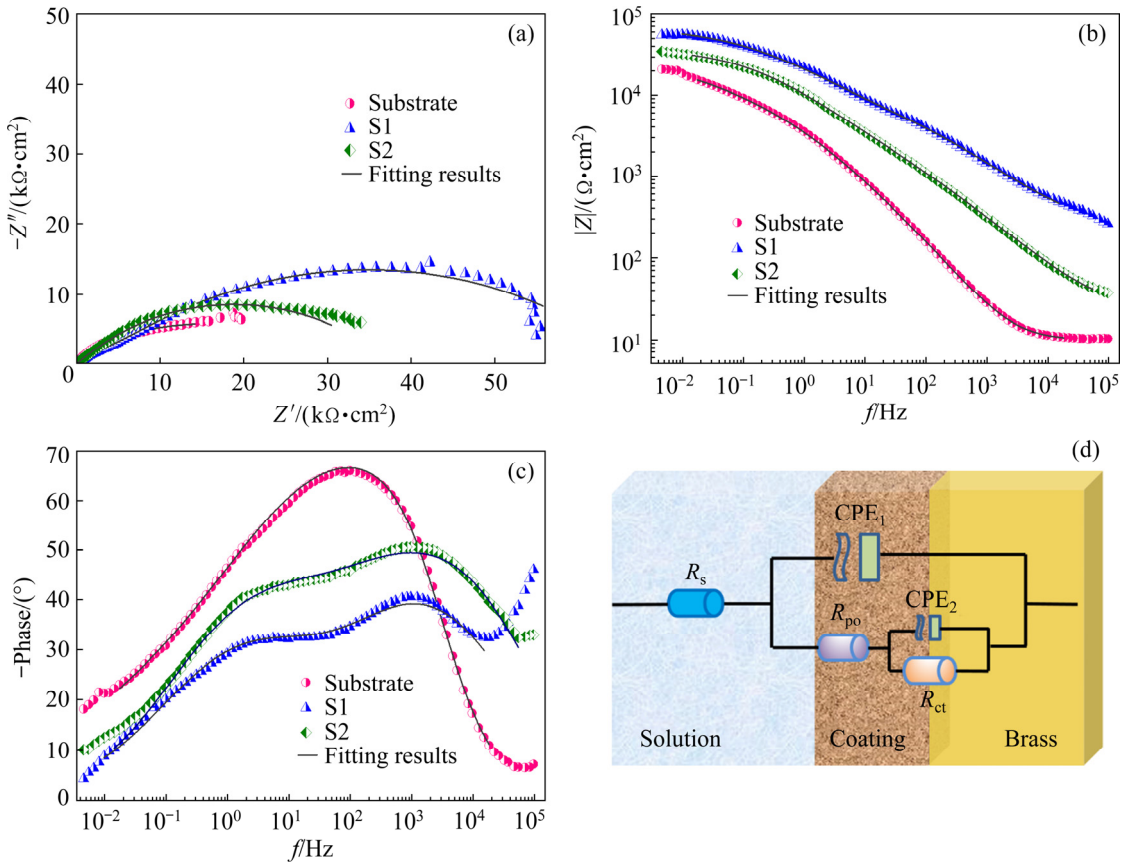

Fig. 8 EIS test results in 3.5 wt.% NaCl solution for uncoated brass and coatings obtained by PEO treatment in S1 and S2 electrolytes for 1200 s: (a) Nyquist plots; (b, c) Bode plots; (d) Equivalent circuit

surface. Therefore, the fitted model is also suitable for the uncoated brass. In Fig. 8(d), the circuit model consists of the solution resistance (R_s) between the working electrode and the reference electrode, the coating resistance also known as the pore resistance (R_{po}), and R_{ct}, which is the Faradaic charge transfer resistance of the metal surface exposed to the solution in the inner pores [2,50,53]. As well, CPE_1 and CPE_2 are the constant phase elements of the oxide and the interface of metal/inner pores, respectively. Due to roughness and defects of surface, CPE reveals the heterogeneous nature of the solid electrode interface and it is also viewed as a non-ideal frequency-independent capacitor [50,54]. The CPE impedance (Z_{CPE}) can be depicted as [2,50]

$$Z_{CPE}=\frac{1}{Y_0(j\omega)^n} \quad (2)$$

where Y_0 is the admittance constant, n is the CPE power-law ($0 \le n \le 1$), j is imaginary part ($j^2=-1$), and ω is the angular frequency ($\omega=2\pi f$) of AC potential.

All the physical parameters in the modeled circuits are well fitted with the experimental data, and the fitted results are presented in Table 4. The coating obtained in S1 electrolyte possesses the largest R_{po} (6.70 kΩ·cm^2) and R_{ct} (59.95 kΩ·cm^2) values, as compared to the uncoated brass and the S2 coating. The results also illustrate that the coating formed in S1 has the best corrosion resistance.

4 Discussion

Previous reports [11,14] revealed that the formation of $AlPO_4$ and $Al_2O_3{\cdot}AlPO_4$ (AAP) layer on the sample surface in the initial stage is a prerequisite for the occurrence of PEO spark discharges on non-valve metals such as carbon steel and copper in phosphate-containing electrolyte. Also, P element has been detected in Area 2 in the initial stage in Fig. 2 (Table 1). Therefore, plasma discharges occur quickly in S1 electrolyte (Fig. 1(a)), which is due to the formation of dense insulating layer (AAP layer) on brass. However, it takes a long time to generate spark discharge in S2 (Part (ii) in Fig. 1(b)). In the case of S2, the AAP layer is absent. However, it is possible that a deposited layer with the component of SiO_2 may be formed [13]. It is possible that the SiO_2 layer does not possess insulating property as good as that of AAP layer. Hence, plasma discharges are delayed in S2 electrolyte. It is also noted in Fig. 1 that the cell potential surges rapidly to high values in S1, but it exhibits a slowly rising process in S2. This phenomenon also reflects different insulating properties of the formed layers at the initial PEO stage. As known in Ref. [11], $AlPO_4$ is electrically neutral and highly covalent, and it is also chemically inert and has high thermal stability. It may be that the initial SiO_2 layer in S2 is not as dense as the AAP layer in S1 and is formed gradually, which causes the potential to rise slowly in Fig. 1(b).

A black coating is formed in S1 electrolyte and a reddish coating is formed in S2 electrolyte. This is because the Cu species in coating prepared in S1 electrolyte exist mostly in the form of CuO, while Cu_2O is dominant in the coating prepared in S2. The XPS data also corroborate this result. In Fig. 5(a), we only find the Cu_2O peak, but no CuO and its satellite peaks are found, indicating that there is no or very little CuO on the surface of the coating prepared in the S2 electrolyte. Besides, the PEO coatings of brass formed in pure silicate also show a reddish color, which may be the characteristic of PEO coatings of brass in silicate electrolyte [13]. Also, it is beneficial to converting CuO to Cu_2O at high temperatures, as shown in the following reaction:

$$4CuO \rightarrow 2Cu_2O+O_2\uparrow \quad (3)$$

As we know, the plasma electron temperature

Table 4 EIS fitted parameters of uncoated brass and coatings formed in S1 and S2 electrolytes

Sample	R_s/ (Ω·cm^2)	Y_0 for CPE_1 ($\Omega^{-1}\cdot s^{-n}\cdot cm^{-2}$)	n for CPE_1	R_{po}/ (kΩ·cm^2)	Y_0 for CPE_2/ ($\Omega^{-1}\cdot s^{-n}\cdot cm^{-2}$)	n for CPE_2	R_{ct}/ (kΩ·cm^2)
Brass	9.84	2.66×10^{-5}	0.84	0.092	8.67×10^{-5}	0.37	35.34
S1 coating	213.30	4.04×10^{-6}	0.58	6.70	1.45×10^{-5}	0.49	59.95
S2 coating	21.96	1.28×10^{-5}	0.63	2.77	1.98×10^{-5}	0.50	34.78

during the PEO processing can be as high as 7000 K [13,14], which may favor the formation of Cu_2O. However, the same high temperature condition exists during the PEO in S1 solution, and the difference in the relative contents of CuO and Cu_2O in the two electrolytes may deserve further study.

5 Conclusions

(1) In S1 electrolyte, a mixed layer of $AlPO_4$ and Al_2O_3 is formed at the initial PEO stage on the brass, which leads to fast establishment of plasma discharges and formation of black coatings with the compositions of Al_2O_3, CuO, Cu_2O and ZnO. In S2 electrolyte, it takes much longer time for the occurrence of plasma discharges and the coatings show a reddish color which is due to the Cu_2O formation on the coating surface.

(2) The Mott−Schottky tests found that in S1 electrolyte, the coatings are mainly p-type semiconductor; while in S2 electrolyte, the semiconductor type of the coatings can be adjusted between n-type and p-type as potential changes.

(3) The potentiodynamic polarization and electrochemical impedance spectroscopy (EIS) tests show that the PEO treatment can significantly improve the corrosion resistance of the brass, with corrosion protection efficiency of 91.50% (S1 coatings) and 90.92 % (S2 coatings).

Acknowledgments

This work is supported by the National Natural Science Foundation of China (No. 51671084) and the Postgraduate Scientific Research Innovation Project of Hunan Province, China (No. QL20210092).

References

[1] ALAM M A, YA H H, AHMAD A, YUSUL M, AZEEM M, MASOOD F. Influence of aluminum addition on the mechanical properties of brass/Al composites fabricated by stir casting [J]. Materials Today: Proceedings, 2022, 48: 811−814.

[2] MOUSAVI S E, NAGHSHEHKESH N, AMIRNEJAD M, SHAMMAKHI H, SONBOLI A. Corrosion performance and tribological behavior of diamond-like carbon based coating applied on Ni−Al−bronze alloy [J]. Transactions of Nonferrous Metals Society of China, 2021, 31(2): 499−511.

[3] HUANG Guo-qiang, FENG Xiao-mei, SHEN Yi-fu, ZHENG Qix-xian, ZHAO Peng-cheng. Friction stir brazing of 6061 aluminum alloy and H62 brass: Evaluation of microstructure, mechanical and fracture behavior [J]. Materials & Design, 2016, 99: 403−411.

[4] KHEZRI M, REZAI B, ABDOLLAHZADEH A A, WILSON B P, MOLAEINASAB M, LUNDSTRÖM M. Cyclic voltammetry and potentiodynamic polarization studies of chalcopyrite concentrate in glycine medium [J]. Transactions of Nonferrous Metals Society of China, 2021, 31(2): 545−554.

[5] CHENG Ying-liang, XUE Zhi-gang, WANG Qun, WU Xiang-quan, MATYKINA E, SKELDON P, THOMPSON G E. New findings on properties of plasma electrolytic oxidation coatings from study of an Al−Cu−Li alloy [J]. Electrochimica Acta, 2013, 107: 358−378.

[6] TU Wen-bin, CHENG Yu-lin, WANG Xin-yao, ZHAN Ting-yan, HAN Jun-xiang, CHENG Ying-liang. Plasma electrolytic oxidation of AZ31 magnesium alloy in aluminate−tungstate electrolytes and the coating formation mechanism [J]. Journal of Alloys and Compounds, 2017, 725: 199−216.

[7] HAN Jun-xiang, CHENG Yu-lin, TU Wen-bin, ZHAN Ting-yan, CHENG Ying-liang. The black and white coatings on Ti−6Al−4V alloy or pure titanium by plasma electrolytic oxidation in concentrated silicate electrolyte [J]. Applied Surface Science, 2018, 428: 684−697.

[8] CHENG Ying-liang, WANG Ting, LI Shao-xian, CHENG Yu-lin, CAO Jin-hui, XIE Huan-jun. The effects of anion deposition and negative pulse on the behaviours of plasma electrolytic oxidation (PEO)—A systematic study of the PEO of a Zirlo alloy in aluminate electrolytes [J]. Electrochimica Acta, 2017, 225: 47−68.

[9] CHENG Ying-liang, ZHANG Qin-ghe, ZHU Zhun-da, TU Wen-bin, CHENG Yu-lin, SKELDON P. Potential and morphological transitions during bipolar plasma electrolytic oxidation of tantalum in silicate electrolyte [J]. Ceramics International, 2020, 46(9): 13385−13396.

[10] XIE Huan-jun, CHENG Ying-liang, LI Shao-xian, CAO Jin-hui, CAO Li. Wear and corrosion resistant coatings on surface of cast A356 aluminum alloy by plasma electrolytic oxidation in moderately concentrated aluminate electrolytes [J]. Transactions of Nonferrous Metals Society of China, 2017, 27(2): 336−351.

[11] LI Zhi, CHENG Yu-lin, KANG Shi-hang, TU Wen-bin, CHENG Ying-liang. A re-understanding of the breakdown theory from the study of the plasma electrolytic oxidation of a carbon steel—A non-valve metal [J]. Electrochimica Acta, 2018, 284: 681−695.

[12] WANG Yun-long, JIANG Zhao-hua, YAO Zhong-ping, TANG Hui. Microstructure and corrosion resistance of ceramic coating on carbon steel prepared by plasma electrolytic oxidation [J]. Surface and Coatings Technology, 2010, 204(11): 1685−1688.

[13] CHENG Yu-lin, ZHU Zhun-da, ZHANG Qing-he, ZHUANG Xiu-juan, CHENG Ying-liang. Plasma electrolytic oxidation of brass [J]. Surface and Coatings Technology, 2020, 385: 125366.

[14] CHENG Yu-lin, WEI Bin-jian, LIU Yuan-yuan, CHENG Ying-liang. Plasma electrolytic oxidation of copper in an aluminate based electrolyte with the respective additives of Na_3PO_4, NaH_2PO_4 and NaH_2PO_2 [J]. Applied Surface Science, 2021, 565: 150477.

[15] PENG Jian, CHEN Bi-li, WANG Zhi-chang, GUO Jing, WU Bing-hui, HAO Shu-qiang, ZHANG Qing-hua, GU Lin,

ZHOU Qin, LIU Zhi, HONG Shu-qin, YOU Si-fan, FU An, SHI Zai-fa, XIE Hao, CAO Duan-yun, LIN Chang-jian, FU Gang, ZHENG Lan-sun, JIANG Ying, ZHENG Nan-feng. Surface coordination layer passivates oxidation of copper [J]. Nature, 2020, 586(7829): 390−394.

[16] MKHALID I A, SHAWKY A. Cu-supported Cu_2O nanoparticles: Optimized photodeposition enhances the visible light photodestruction of atrazine [J]. Journal of Alloys and Compounds, 2021, 853: 157040.

[17] ZUBAIR N, AKHTAR K. Morphology controlled synthesis of ZnO nanoparticles for in-vitro evaluation of antibacterial activity [J]. Transactions of Nonferrous Metals Society of China, 2020, 30(6): 1605−1614.

[18] YE Zheng-mao, HU Lei, JIANG Jiang, TANG Jian-xin, CAO Xue-qin, GU Hong-wei. CuO@Ag as a highly active catalyst for the selective oxidation of trans-stilbene and alcohols [J]. Catalysis Science & Technology, 2012, 2(6): 1146−1149.

[19] VATTIKUTI S V P, REDDY B P, BYON C, SHIM J. Carbon/CuO nanosphere-anchored g-C_3N_4 nanosheets as ternary electrode material for supercapacitors [J]. Journal of Solid State Chemistry, 2018, 262: 106−111.

[20] VERMA N, KUMAR N. Synthesis and biomedical applications of copper oxide nanoparticles: An expanding horizon [J]. ACS Biomaterials Science & Engineering, 2019, 5(3): 1170−1188.

[21] WU Wen-ting, ZHAO Wen-jie, WU Ying-hao, ZHOU Cheng-xu, LI Long-yang, LIU Zhi-xiong, DONG Jian-da, ZHOU Kai-he. Antibacterial behaviors of Cu_2O particles with controllable morphologies in acrylic coatings [J]. Applied Surface Science, 2019, 465: 279−287.

[22] XIONG Liang-bin, HUANG Sheng, YANG Xi, QIU Ming-qiang, CHEN Zheng-hua, YU Ying. p-type and n-type Cu_2O semiconductor thin films: Controllable preparation by simple solvothermal method and photoelectrochemical properties [J]. Electrochimica Acta, 2011, 56(6): 2735−2739.

[23] XIE Cong-jia, WANG Wei, YANG Ye-peng, JIANG Liang, CHEN Yong-juan, HE Jiao, WANG Jia-qiang. Enhanced stability and activity for solvent-free selective oxidation of cyclohexane over Cu_2O/CuO fabricated by facile alkali etching method [J]. Molecular Catalysis, 2020, 495: 111134.

[24] CAI Lina, LI Hai-rong, ZHANG Huan, FAN Wen-hao, WANG Jian-an, WANG Yong-chang, WANG Xu-dong, TANG Ying, SONG Yu-zhe. Enhanced performance of the tangerines-like CuO-based gas sensor using ZnO nanowire arrays [J]. Materials Science in Semiconductor Processing, 2020, 118: 105196.

[25] DUOC V T, HUNG C M, NGUYEN H, DUY N V, HIEU N V, HOA N D. Room temperature highly toxic NO_2 gas sensors based on rootstock/scion nanowires of SnO_2/ZnO, ZnO/SnO_2, SnO_2/SnO_2 and, ZnO/ZnO [J]. Sensors and Actuators B: Chemical, 2021, 348: 130652.

[26] ZHU Ling, ZENG Wen. Room-temperature gas sensing of ZnO-based gas sensor: A review [J]. Sensors and Actuators A: Physical, 2017, 267: 242−261.

[27] HEYDARIAN A, ATAPOUR M, HAKIMIZAD A, RAEISSI K. The effects of anodic amplitude and waveform of applied voltage on characterization and corrosion performance of the coatings grown by plasma electrolytic oxidation on AZ91 Mg alloy from an aluminate bath [J]. Surface and Coatings Technology, 2020, 383: 125235.

[28] FERNÁNDEZ-LÓPEZ P, ALVES S A, LÓPEZ-ORTEGA A, JOSÉ-LOMBERA J T S, BAYÓN R. High performance tribological coatings on a secondary cast Al−Si alloy generated by plasma electrolytic oxidation [J]. Ceramics International, 2021, 47(22): 31238−31250.

[29] HAMRAHI B, YARMAND B, MASSOUDI A. Improved in-vitro corrosion performance of titanium using a duplex system of plasma electrolytic oxidation and graphene oxide incorporated silane coatings [J]. Surface and Coatings Technology, 2021, 422: 127558.

[30] YANG Chao, ZHU Jia-yu, CUI Sui-han, CHEN Ping-hu, WU Zhong-can, MA Zheng-yong, FU R K Y, TIAN Xiu-bo, CHU P K, WU Zhong-zhen. Wear and corrosion resistant coatings prepared on LY12 aluminum alloy by plasma electrolytic oxidation [J]. Surface and Coatings Technology, 2021, 409: 126885.

[31] WU Jie, LU Ping, DONG Lei, ZHAO Meng-li, LI De-jun, XUE Wen-bin. Combination of plasma electrolytic oxidation and pulsed laser deposition for preparation of corrosion-resisting composite film on zirconium alloys [J]. Materials Letters, 2020, 262: 127080.

[32] WEI Ke-jian, WANG Xing-ping, ZHU Ming-hao, GUAN Hao-bao, XU Chi, XUE Wen-bin, ZHANG Jin-long. Effects of Li, B and H elements on corrosion property of oxide films on ZIRLO alloy in 300 °C/14 MPa lithium borate buffer solutions [J]. Corrosion Science, 2021, 181: 109216.

[33] ZOU Yong-chun, WANG Ya-ming, WEI Da-qing, DU Qing, OUYANG Jia-hu, JIA De-chang, ZHOU Yu. In-situ SEM analysis of brittle plasma electrolytic oxidation coating bonded to plastic aluminum substrate: Microstructure and fracture behaviors [J]. Materials Characterization, 2019, 156: 109851.

[34] GE Yu-lin, WANG Ya-ming, CUI Yi, ZOU Yong-chun, GUO Li-xin, OUYANG Jia-hu, JIA De-chang, ZHOU Yu. Growth of plasma electrolytic oxidation coatings on Nb and corresponding corrosion resistance [J]. Applied Surface Science, 2019, 491: 526−534.

[35] HUSSEIN R O, NIE X, NORTHWOOD D O. Influence of process parameters on electrolytic plasma discharging behaviour and aluminum oxide coating microstructure [J]. Surface and Coatings Technology, 2010, 205(6): 1659−1667.

[36] KALKANCI H, KURNAZ S C. The effect of process parameters on mullite-based plasma electrolytic oxide coatings [J]. Surface and Coatings Technology, 2008, 203(1/2): 15−22.

[37] GULEC A E, GENCER Y, TARAKCI M. The characterization of oxide based ceramic coating synthesized on Al−Si binary alloys by microarc oxidation [J]. Surface and Coatings Technology, 2015, 269: 100−107.

[38] ZHU Zhun-da, TU Wen-bin, CHENG Yu-lin, CHENG Ying-liang. The formation of metallic W and amorphous phase in the plasma electrolytic oxidation coatings on an Al alloy from tungstate-containing electrolyte [J]. Surface and Coatings Technology, 2019, 361: 176−187.

[39] BIESINGER M C, LAU L W M, GERSON A R, SMART R S C. Resolving surface chemical states in XPS analysis of first row transition metals oxides and hydroxides: Sc, Ti, V, Cu and Zn [J]. Applied Surface Science, 2010, 257: 887−898.

[40] BARR T L, YIN Meng-ping, VARMA S. Detailed x-ray photoelectron spectroscopy valence band and core level

studies of select metals oxidations [J]. Journal of Vacuum Science & Technology A, 1992, 10(4): 2383−2390.
[41] ZHAO Chen, FU Hai-tao, YANG Xiao-hong, XIONG Shi-xian, HAN De-zhi, AN Xi-zhang. Adsorption and photocatalytic performance of Au nanoparticles decorated porous Cu_2O nanospheres under simulated solar light irradiation [J]. Applied Surface Science, 2021, 545: 149014.
[42] HARTNEY M A, CHIANG J N, HESS D W, SOANE D S. Oxide formation during plasma etching of silicon containing resists [J]. Applied Physics Letters, 1989, 54(16): 1510−1512.
[43] AGUILERA L, FAGUNDES N, MELO A D, BANDEIRA B, NOBRE F X, ANGLADA-RIVERA J, SILVA J P, CRUZ J P D L, LEYET Y. Influence of sonication time on the structure and electrical properties of $Na_2Ti_6O_{13}$ ceramics: An approach applying the Mott−Schottky model [J]. Ceramics International, 2020, 46(7): 8706−8710.
[44] ADÁN-MÁS A, SILVA T M, GUERLOU-DEMOURGUES L, MONTEMOR M F. Application of the Mott−Schottky model to select potentials for EIS studies on electrodes for electrochemical charge storage [J]. Electrochimica Acta, 2018, 289: 47−55.
[45] WEI Ke-jian, WANG Xing-ping, LI Jian-hui, QU Yao, WAN Xu-min, DU Jian-cheng, XUE Wen-bin. In-situ electrochemical study of plasma electrolytic oxidation treated Zr_3Al based alloy in 300 °C/14 MPa lithium borate buffer solution [J]. Thin Solid Films, 2020, 707: 138066.
[46] KIM C L, CHUNG W J, LEE J Y. Design of hole transport type host for stable operation in blue organic light-emitting diodes [J]. Organic Electronics, 2020, 82: 105724.
[47] AMEGROUD H, GUENBOUR A, BELLAOUCHOU A, AOUFIR Y E, LGAZ H, CHUNG I M. A comprehensive investigation of the electrochemical behavior of nickel−aluminum bronze alloy in alkaline solution: The effect of film formation potential [J]. Colloids and Surfaces A: Physicochemical and Engineering Aspects, 2021, 614: 126126.
[48] YI Pan, DONG Chao-fang, XIAO Kui, MAN Cheng, LI Xiao-gang. In-situ investigation of the semiconductive properties and protective role of Cu_2O layer formed on copper in a borate buffer solution [J]. Journal of Electroanalytical Chemistry, 2018, 809: 52−58.
[49] CHENG Yu-lin, ZHANG Qing-he, CHENG Ying-liang. Corrosion-resistant coatings on tantalum formed by plasma electrolytic oxidation in phosphate electrolyte [J]. Surface Technology, 2021, 50(6): 32−40.
[50] CHUKWUIKE V I, PRASANNAKUMAR R S, GNANASEKAR K, BARIK R C. Copper corrosion mitigation: A new insight for fabricating a surface barrier film against chloride ion under hydrodynamic flow [J]. Applied Surface Science, 2021, 555: 149703.
[51] LIU Z Y, LI X G, CHENG Y F. Understand the occurrence of pitting corrosion of pipeline carbon steel under cathodic polarization [J]. Electrochimica Acta, 2012, 60: 259−263.
[52] NAM N D, BUI Q V, NHAN H T, PHUONG D V, BIAN M Z. Effect of Pd interlayer on electrochemical properties of ENIG surface finish in 3.5 wt.% NaCl solution [J]. Journal of Electronic Materials, 2014, 43(16): 3307−3316.
[53] XU Shi-yuan, LIU Chu-ming, WAN Ying-chun, ZHENG Guang, CAO Yong-hao, JIANG Shu-nong. Corrosion behaviour of Mg−Gd−Y−Zn−Ag alloy components with different sizes after cooling [J]. Transactions of Nonferrous Metals Society of China, 2021, 31(5): 1291−1302.
[54] NEZAMDOUST S, SEIFZADEH D, HABIBI-YANGJEH A. Nanodiamond incorporated sol−gel coating for corrosion protection of magnesium alloy [J]. Transactions of Nonferrous Metals Society of China, 2020, 30(6): 1535−1549.

黄铜在含磷酸二氢钠或硅酸钠的铝酸盐电解液中的等离子电解氧化行为和耐腐蚀性能

程昱琳，冯 恬，吕佳慧，胡攀峰，程英亮

湖南大学 材料科学与工程学院，长沙 410082

摘 要：采用等离子电解氧化(PEO)技术对黄铜进行表面处理，研究其在铝酸盐电解液中分别加入 NaH_2PO_4 (S1)和 Na_2SiO_3 (S2)添加剂对涂层形成和耐腐蚀性能的影响。在 S1 电解液中进行 PEO 处理的初始阶段，黄铜表面形成 $AlPO_4$ 和 Al_2O_3 的混合涂层，导致快速产生等离子体火花放电现象并形成由 Al_2O_3、CuO、Cu_2O 和 ZnO 组成的黑色涂层。然而，在 S2 电解液中，等离子体火花放电行为延迟产生。由于产生较多的 Cu_2O，S2 涂层显示为深红棕色。Mott−Schottky 测试表明，S1 涂层为 p 型半导体；S2 涂层具有 n 型和 p 型半导体可调性。动电位极化和电化学阻抗谱(EIS)测试表明，PEO 处理能显著提高黄铜的耐腐蚀性，腐蚀防护效率可达 91.50%，S1 涂层电荷转移电阻最大可达 59.95 kΩ·cm^2。

关键词：等离子体电解氧化；黄铜；耐腐蚀性能；铝酸盐；磷酸二氢钠；硅酸钠

(Edited by Wei-ping CHEN)